

ON THE UNIVERSAL LATE X-RAY EMISSION OF BINARY-DRIVEN HYPERNOVAE AND ITS POSSIBLE COLLIMATION

G. B. PISANI^{1,2}, R. RUFFINI^{1,2,3,4}, Y. AIMURATOV^{1,3}, C. L. BIANCO^{1,2}, M. KOVACEVIC^{1,3}, R. MORADI^{1,2}, M. MUCCINO^{1,2},
A. V. PENACCHIONI^{5,6}, J. A. RUEDA^{1,2,4}, S. SHAKERI^{2,7}, Y. WANG^{1,2}

Draft version September 11, 2018

ABSTRACT

It has previously been discovered that there is a universal power law behavior exhibited by the late X-ray emission (LXRE) of a “golden sample” (GS) of six long energetic GRBs, when observed in the rest-frame of the source. This remarkable feature, independent of the different isotropic energy (E_{iso}) of each GRB, has been used to estimate the cosmological redshift of some long GRBs. This analysis is extended here to a new class of 161 long GRBs, all with $E_{iso} > 10^{52}$ erg. These GRBs are indicated as binary-driven hypernovae (BdHNe) in view of their progenitors: a tight binary system composed of a carbon-oxygen core (CO_{core}) and a neutron star undergoing an induced gravitational collapse (IGC) to a black hole triggered by the CO_{core} explosion as a supernova (SN). We confirm the universal behavior of the LXRE for the “enlarged sample” (ES) of 161 BdHNe observed up to the end of 2015, assuming a double-cone emitting region. We obtain a distribution of half-opening angles peaking at $\theta = 17.62^\circ$, with a mean value of 30.05° , and a standard deviation of 19.65° . This, in turn, leads to the possible establishment of a new cosmological candle. Within the IGC model, such universal LXRE behavior is only indirectly related to the GRB and originates from the SN ejecta, of a standard constant mass, being shocked by the GRB emission. The fulfillment of the universal relation in the LXRE and its independence of the prompt emission, further confirmed in this article, establishes a crucial test for any viable GRB model.

Keywords: supernovae: general — binaries: general — gamma-ray burst: general — stars: neutron

1. INTRODUCTION

The initial observations by the BATSE instrument on board the Compton γ -ray Observatory satellite have evidenced what has later become known as the prompt radiation of GRBs. On the basis of their hardness as well as their duration, GRBs were initially classified into short and long at a time when their cosmological nature was still being disputed (Mazets et al. 1981; Klebesadel 1992; Dezalay et al. 1992; Kouveliotou et al. 1993; Tavani 1998).

The advent of the *BeppoSAX* satellite (Boella et al. 1997) introduced a novel approach to GRBs by introducing joint observations in the X-rays and γ -rays thanks to its instruments: the Gamma-ray Burst Monitor (40–700 keV), the Wide Field Cameras (2–26 keV), and the Narrow Field Instruments (2–10 keV). The unexpected and welcome discovery of the existence of a well separate component in the GRB soon appeared: the afterglow radiation lasting up to 10^5 – 10^6 s after the emission of the prompt radiation (see Costa et al. 1997a,b; Frontera et al. 1998, 2000; de Pasquale et al. 2006). *BeppoSAX* clearly indicated the existence of a power law behavior

in the late X-ray emission (LXRE; see Fig. 1).

The coming of the *Swift* satellite (Gehrels et al. 2004; Evans et al. 2007, 2010), significantly extending the observation in the X-ray band thanks to its X-ray Telescope (XRT band: 0.3–10 keV), has allowed us for the first time to cover the unexplored region between the end of the prompt radiation and the power law late X-ray behavior discovered by *BeppoSAX*: in some long GRBs a steep decay phase was observed followed by a plateau leading then to a typical LXRE power law behavior (Evans et al. 2007, 2010).

Already, Pisani et al. (2013) noticed the unexpected result that the LXREs of a “golden sample” (GS) of six long, closeby ($z \lesssim 1$), energetic ($E_{iso} > 10^{52}$ erg) GRBs, when measured in the rest-frame of the sources, were showing a common power law behavior (see Fig. 2), independently from the isotropic energy E_{iso} coming from the prompt radiation (see Fig 3). More surprising was the fact that the plateau phase luminosity and duration before merging in the common LXRE power law behavior were clearly functions of the E_{iso} (see Fig. 3, and Ruffini et al. 2014c), while the late power law remains independent from the energetic of the prompt radiation (see Fig. 2–3, and Pisani et al. 2013; Ruffini et al. 2014c). For this reason, this remarkable scaling law has been used as a standard candle to independently estimate the cosmological redshift of some long GRBs by requiring the overlap of their LXRE (see, e.g., Penacchioni et al. 2012, 2013; Ruffini et al. 2013b,c, 2014a), and also to predict, 10 days in advance, the emergence of the typical optical signature of the supernova SN 2013cq, associated with GRB 130427A (Ruffini et al. 2015, 2013a; de Ugarte Postigo et al. 2013; Levan et al. 2013).

¹ Dipartimento di Fisica, Sapienza Università di Roma and ICRA, Piazzale Aldo Moro 5, I-00185 Roma, Italy

² ICRA Net, Piazza della Repubblica 10, I-65122 Pescara, Italy

³ Université de Nice Sophia-Antipolis, Grand Château Parc Valrose, Nice, CEDEX 2, France

⁴ ICRA Net-Rio, Centro Brasileiro de Pesquisas Fisicas, Rua Dr. Xavier Sigaud 150, Rio de Janeiro, RJ, 22290-180, Brazil

⁵ University of Siena, Department of Physical Sciences, Earth and Environment, Via Roma 56, I-53100 Siena, Italy

⁶ ASI Science Data Center, via del Politecnico s.n.c., I-00133 Rome Italy

⁷ Department of Physics, Isfahan University of Technology, Isfahan 84156-83111, Iran

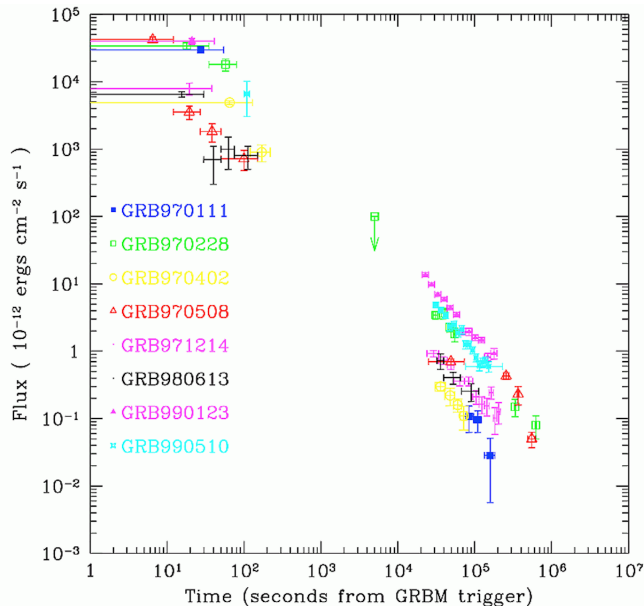


Figure 1. Collection of X-ray afterglow light curves observed by the Italian-Dutch satellite *BeppoSAX*.

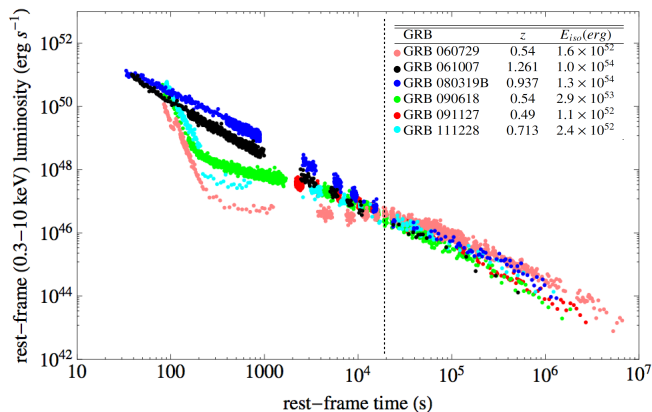


Figure 2. Scaling law found in the isotropic X-ray late times luminosity within the GS by Pisani et al. (2013). Despite the different early behavior, the different light curves join all together the same power law after a rest-frame time of $t_{rf} \sim 2 \times 10^4$ s.

The current analysis is based on the paradigms introduced in Ruffini et al. (2001a) for the spacetime parametrization of the GRBs, in Ruffini et al. (2001b) for the interpretation of the structure of the GRB prompt emission, and in Ruffini et al. (2001c) for the induced gravitational collapse (IGC) process, further evolved in Ruffini et al. (2007), Rueda & Ruffini (2012), Fryer et al. (2014), and Ruffini et al. (2016c). In the present case, the phenomenon points to an IGC occurring when a tight binary system composed of a carbon-oxygen core (CO_{core}) undergoes a supernova (SN) explosion in the presence of a binary neutron star (NS) companion (Ruffini et al. 2001b, 2007; Izzo et al. 2012a; Rueda & Ruffini 2012; Fryer et al. 2014; Ruffini et al. 2015). When the IGC leads the NS to accrete enough matter and therefore to collapse to a black hole (BH), the overall observed phenomenon is called binary-driven hypernova (BdHN; Fryer et al. 2014; Ruffini et al. 2015, 2016c).

A crucial further step has been the identification as a BdHN of GRB 090423 (Ruffini et al. 2014b) at the

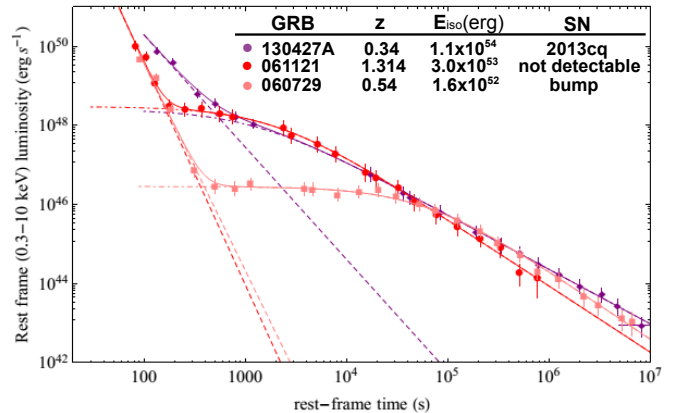


Figure 3. Nested structure of the isotropic X-ray luminosity of the BdHNe. This includes the previously mentioned scaling law of the late power law and leads to an inverse proportionality between the luminosity of the plateau and the rest-frame time delimiting its end and the beginning of the late power-law decay Ruffini et al. (2014c).

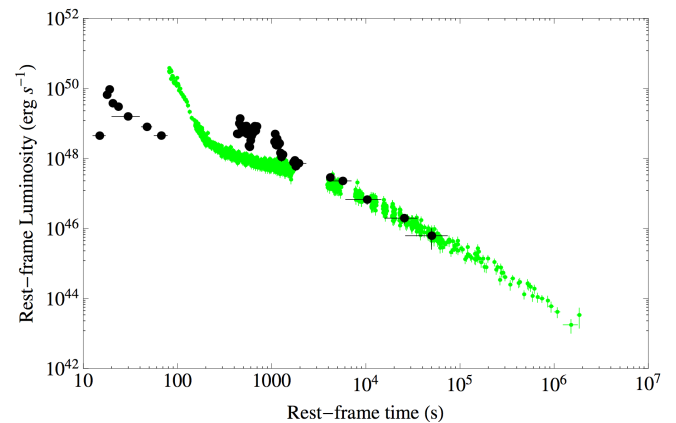


Figure 4. X-ray luminosity of GRB 090423 (black points) compared with the one of GRB 090618 (green points), the prototype BdHN, by Ruffini et al. (2014b).

extreme redshift of $z = 8.2$ (Salvaterra et al. 2009; Tanvir et al. 2009). On top of that, the LXRE of GRB 090423 overlaps perfectly with the ones of the GS (see Fig. 4), extending such a scaling law up to extreme cosmological distances. This result led to the necessity of checking such a universal behavior of the LXREs in BdHNe at redshifts larger than $z \sim 1$ (see the sample list in Table 2).

It is clear by now that the afterglow analysis is much more articulated than previously expected and contains new specific signatures. When theoretically examined within our framework, these new signatures lead to specific information on the astrophysical nature of the progenitor systems (Ruffini et al. 2016c). In the present paper, we start by analysing the signatures contained in the LXREs at $t_{rf} \gtrsim 10^4$ s, where t_{rf} is the rest-frame time after the initial GRB trigger. In particular, we probe a further improvement for the existence of such an LXRE universal behavior of BdHNe by the introduction of a collimation correction.

In Section 2 we present an “enlarged sample” (ES) of 161 BdHNe observed up to the end of 2015. In particular, we express for each BdHN: (1) redshift; (2) E_{iso} ; and (3) the LXRE power law properties. We probe the uni-

versality of the LXRE power law behavior as well as the absence of correlation with the prompt radiation phase of the GRB. In Section 3 we introduce the collimation correction for the LXRE of BdHNe. This, in turn, will aim to the possible establishment of a new cosmological candle, up to $z \gtrsim 8$. In Section 4 we present the inferences for the understading of the afterglow structure, and, in Section 5, we draw our conclusions.

2. THE BDHNE ENLARGED SAMPLE

We have built a new sample of BdHNe, which we name “enlarged sample” (ES), under the following selection criteria:

- measured redshift z ;
- GRB rest-frame duration larger than 2 s;
- isotropic energy E_{iso} larger than 10^{52} erg; and
- presence of associated *Swift*/XRT data lasting at least up to $t_{rf} = 10^4$ s.

We collected 161 sources, which satisfy our criteria, covering 11 years of *Swift*/XRT observations, up to the end of 2015, see Table 2. The E_{iso} of each source has been estimated using the measured redshift z together with the best-fit parameters of the γ -ray spectrum published in the GCN circular archive⁸. The majority of the ES sources, 102 out of 161, have γ -ray data provided by *Fermi*/GBM and Konus-WIND, which, with their typical energy bands being 10–1000 keV and 20–2000 keV, respectively, lead to a reliable estimate of the E_{iso} , computed in the “bolometric” 1– 10^4 keV band (Bloom et al. 2001). The remaining sources of the ES have had their γ -ray emission observed by *Swift*/BAT only, with the sole exception of one source observed by HETE. The energy bands of these last two detectors, being 15–150 keV and 8–400 keV, respectively, lead to a standard estimate of E_{iso} by extrapolation in the “bolometric” 1– 10^4 keV band (Bloom et al. 2001).

We compare the *Swift*/XRT isotropic luminosity light curve L_{rf}^{iso} for 161 GRBs of the ES in the common rest-frame energy range of 0.3–10 keV. We initially convert the observed *Swift*/XRT flux f_{obs} as if it had been observed in the 0.3–10 keV rest-frame energy range. In the detector frame, the 0.3–10 keV rest-frame energy range becomes $[0.3/(1+z)] - [10/(1+z)]$ keV, where z is the redshift of the GRB. We assume a simple power law function as the best fit for the spectral energy distribution of the *Swift*/XRT data⁹:

$$\frac{dN}{dA dt dE} \propto E^{-\gamma}. \quad (1)$$

Therefore, we can compute the flux light curve in the 0.3–10 keV rest-frame energy range, f_{rf} , multiplying the observed one, f_{obs} , by the k-correction factor:

$$f_{rf} = f_{obs} \frac{\int_{\frac{0.3 \text{ keV}}{1+z}}^{\frac{10 \text{ keV}}{1+z}} E^{1-\gamma} dE}{\int_{0.3 \text{ keV}}^{10 \text{ keV}} E^{1-\gamma} dE} = f_{obs} (1+z)^{\gamma-2}. \quad (2)$$

⁸ http://gcn.gsfc.nasa.gov/gcn3_archive.html

⁹ <http://www.swift.ac.uk/>

Then, to compute the isotropic X-ray luminosity L_{iso} , we have to multiply f_{rf} by the spherical surface having the luminosity distance as radius

$$L_{iso} = 4 \pi d_l^2(z) f_{rf}, \quad (3)$$

where we assume a standard cosmological Λ CDM model with $\Omega_m = 0.27$ and $\Omega_\Lambda = 0.73$. Finally, we convert the observed times into rest-frame times t_{rf} :

$$t_{rf} = \frac{t_{obs}}{1+z}. \quad (4)$$

We then fit the whole isotropic luminosity light-curve late phase with a decaying power law function defined as follows:

$$L_{iso}(t_{rf}) = L_0 t_{rf}^{-\alpha}, \quad (5)$$

where α , the power law index, is a positive number, and L_0 is the luminosity at an arbitrary time $t_{rf} = t_0$ after the GRB trigger in the rest-frame of the source. All the power laws are shown in Fig. 5b. Fig. 6a shows the distribution of the α indexes within the ES. Such a distribution follows a Gaussian behavior with a mean value of $\mu_\alpha = 1.48$ and a standard deviation of $\sigma_\alpha = 0.32$. The LXRE luminosity light curves of the ES in the 0.3–10 keV rest-frame energy band are plotted in Fig. 5a, compared to the curves of the GS. Fig. 5a shows that the power laws within the ES span around two orders of magnitude in luminosity. The spread of the LXRE light curves in the ES is better displayed by Fig. 6b which shows the distribution within the ES of the LXRE integrated energies E_{LT} defined as:

$$E_{LT} \equiv \int_{10^4 \text{ s}}^{10^6 \text{ s}} L_{iso}(t_{rf}) dt_{rf}. \quad (6)$$

We choose to represent the spread of the LXRE luminosity light curves with the late integrated energy E_{LT} at late times ($t_{rf} = 10^4$ – 10^6 s) instead of the luminosity L_{iso} at a particular time for two reasons: (1) there is no evidence for a particular time in which to compute L_{iso} and (2) we want to have a measurement of the spread as much as possible independent from the slopes, whose dispersion causes the mixing of part of the light curves over time (see Fig. 5b). The integration time interval $t_{rf} = 10^4$ – 10^6 reasonably contains most of the data in the late power law behavior. In fact, the lower limit $t_{rf} = 10^4$ s is basically the average of the initial time for our linear fits on the data (more precisely $t_{rf}^{start} = 9167.13$ s), while the upper limit $t_{rf} = 10^6$ has been chosen because only 14% of the ES have X-ray data over such rest-frame time.

The solid red line in Fig. 6b represents the Gaussian function that best fits the late integrated energies E_{LT} in logarithmic scale. Its mean value is $\mu_{\text{Log}_{10}(E_{LT})} = 51.40$, while its standard deviation is $\sigma_{\text{Log}_{10}(E_{LT})} = 0.47$.

The LXRE power-law spread, given roughly by $2\sigma_{\text{Log}_{10}(E_{LT})} = 0.94$, is larger in respect to the previous work of Pisani et al. (2013), which results as $2\sigma_{\text{Log}_{10}(E_{LT})} = 0.56$. This is clearly due to the significant growth of the number of BdHNe composing the ES (161) in respect to the ones of the GS (6).

Furthermore, Fig. 6c-d show the scatter plots of the values of α and E_{LT} , respectively, versus the values of the E_{iso} for all the sources of the ES. In both cases the

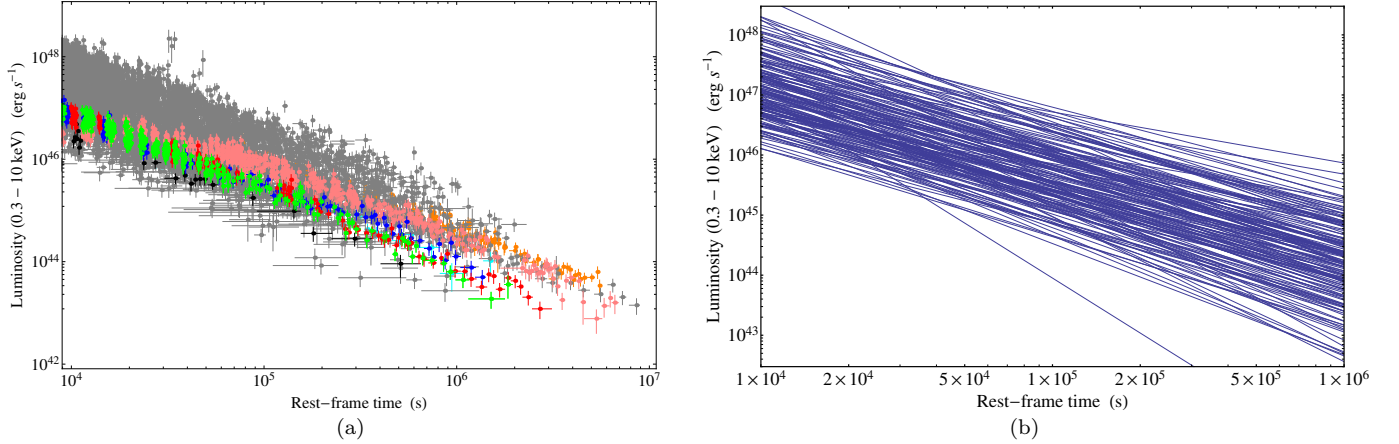


Figure 5. Panel (a): LXRE luminosity light curves of all 161 sources of the ES (gray) compared with the ones of the GS: GRB 060729 (pink), GRB 061007 (black), GRB 080913B (blue), GRB 090618 (green), GRB 091127 (red), and GRB 111228 (cyan), plus GRB 130427A (orange; Pisani et al. 2013; Ruffini et al. 2015). Panel (b): power laws which best fit the luminosity light curves of the X-ray emissions of all 161 sources of the ES.

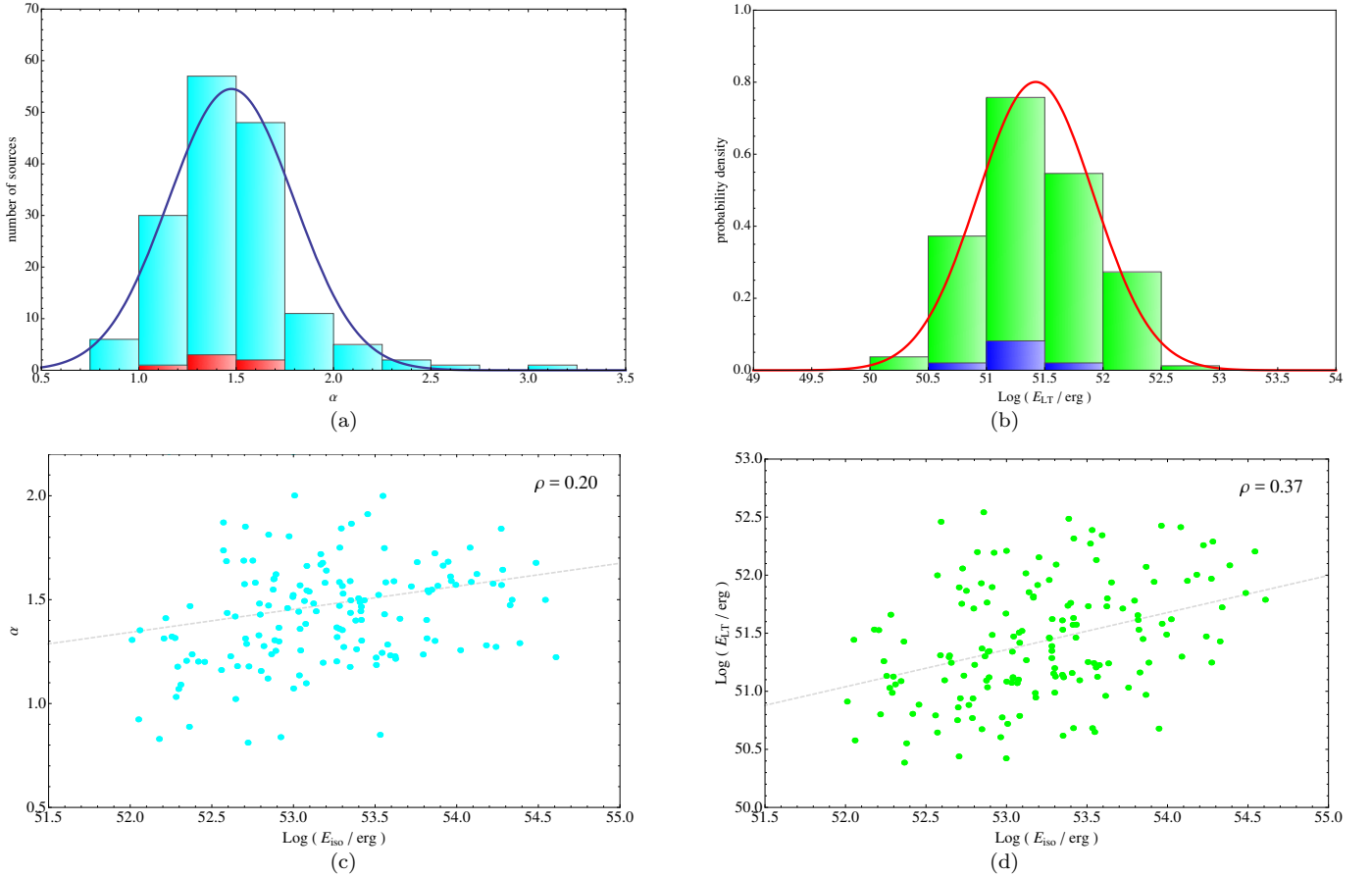


Figure 6. Panel (a): distribution of the LXRE power law indexes α within the ES (cyan) compared to the one of the GS (red). Such a distribution follows a Gaussian behavior (blue line) with a mean value of $\mu_\alpha = 1.48$ and a standard deviation of $\sigma_\alpha = 0.32$. Panel (b): probability distribution of the LXRE integrated energies within the time interval 10^4 – 10^6 s in the rest-frame after the initial GRB trigger for all the sources of the ES (in green) compared with the GS (in blue). The solid red line represents the Gaussian function which best fits the ES data in logarithmic scale. Its mean value is $\mu_{\text{Log}_{10}(E_{LT})} = 51.40$, while its standard deviation is $\sigma_{\text{Log}_{10}(E_{LT})} = 0.47$. Panel (c): scatter plot of α versus E_{iso} (cyan points) in logarithmic scale. The dashed gray line is the best linear fit on such points. If we look at the correlation coefficient of these data points, $\rho = 0.20$, we conclude that there is no evidence for correlation between the two quantities. Panel (d): scatter plot of E_{LT} versus E_{iso} (green points) in logarithmic scale. The dashed gray line is the best linear fit on such points. If we look at the correlation coefficient of these data points, $\rho = 0.37$, we conclude that there is no evidence for correlation between the two quantities.

correlation factors, $\rho = 0.20$ and $\rho = 0.37$ respectively, are low, confirming that there is no evidence for a correlation between the LXRE power law behavior and the isotropic energy emitted by the source during the prompt radiation.

These results address a different aspect than the ones by Margutti et al. (2013). There, the authors, after correctly noticing the difficulties of the traditional afterglow model (Meszaros & Rees 1997; Sari et al. 1998), attempt to find a model-independent correlation between the X-ray light curve observed in both short and long GRBs with their prompt emission. In their work, Margutti et al. (2013) have considered the integrated X-ray emission over the entire light curve observed by XRT, following ~ 300 s after the GRB trigger both for short and long GRBs. Such an emission is clearly dominated by the contribution at $t_{rf} < 10^4$ s, where a dependence from the E_{iso} is self-evident from the above Fig. 2 and Fig. 3. Our approach instead solely applies to the BdHNe: (1) long GRBs, and (2) $E_{iso} > 10^{52}$ erg. This restricts the possible sources in the Margutti et al. (2013) sample to 70 GRBs: in the present article, we consider a larger sample of 161 BdHNe. Moreover, (3) our temporal window starts at $t_{rf} \gtrsim 10^4$ s. Under these three conditions, our result of the universal LXRE behavior has been found.

3. COLLIMATION

We here propose to reduce the spread of the LXRE power laws within the ES by introducing a collimation effect in the emission process. In fact, if the emission is not isotropic, Fig. 5a-b should actually show overestimations of the intrinsic LXRE luminosities. By introducing a collimation effect, namely assuming that the LXREs are not emitted isotropically but within a double-cone region having half-opening angle θ , we can convert the isotropic $L_{iso}(t_{rf})$ to the intrinsic LXRE luminosity $L^{intr}(t_{rf})$ as:

$$L^{intr}(t_{rf}) = L_{iso}(t_{rf}) (1 - \cos \theta). \quad (7)$$

From Eq. 7, an angle θ can be inferred for each source of the ES if an intrinsic universal LXRE light curve $L^{intr}(t_{rf})$ is assumed. For example, assuming an intrinsic standard luminosity L_0^{intr} , at an arbitrary time $t_{rf} = t_0$, Eq. 7 becomes $L_0^{intr} = L_0 (1 - \cos \theta)$, which, in principle, could be used to infer θ for each source. On the other hand, for the same reasons expressed in the previous section, we choose to estimate the angles θ using the LXRE integrated energy E_{LT} instead of the L_{iso} at a particular time. Therefore, we simply integrate Eq. 7 in the rest-frame time interval 10^4 – 10^6 s:

$$\int_{10^4 s}^{10^6 s} L^{intr}(t_{rf}) dt_{rf} = \int_{10^4 s}^{10^6 s} L_{iso}(t_{rf}) (1 - \cos \theta) dt_{rf}, \quad (8)$$

obtaining, consequentially

$$E_{LT}^{intr} = E_{LT} (1 - \cos \theta). \quad (9)$$

By assuming a universal E_{LT}^{intr} for all BdHNe, it is possible to infer θ for each source of the ES. We assume GRB 050525A, having the lowest E_{LT} within the ES, as our unique “isotropic” source, namely, in which we can impose $E_{LT}^{intr} = E_{LT}$, which automatically gives

$\theta = 90^\circ$, which means that the LXRE luminosity is emitted over all the isotropic sphere. On the top of having the weakest LXRE over 11 years of *Swift*/XRT observations, GRB 050525A: (a) has been observed by Konus-WIND in the γ -rays (Golenetskii et al. 2005), then its E_{iso} estimate is reliable; (b) has a reliable late X-ray slope given by a complete *Swift*/XRT light curve (showing a late power law behavior from 4000 to 7×10^5 s in the rest frame); (c) has an associated supernova (Della Valle et al. 2006b,a). An instrumental selection effect cannot affect this choice since *Swift*/XRT can easily detect and follow X-ray emissions weaker than that of GRB 050525A. Some examples are the two X-ray luminosity light curves shown of GRB 060218 and GRB 101219B in Fig. 8-a. Furthermore, in the case of a future observation of a BdHN showing a E_{LT} weaker than the one of GRB 050525A, a renormalization of the angle distribution of Fig. 7a down to lower angle values with respect to the new minimum one would be required, leaving the overall angle distribution unaltered. All of these facts make GRB 050525A a robust “isotropic” BdHN candidate. With $E_{LT}^{intr} = E_{LT}^{050525A} = 2.43 \times 10^{50}$ now fixed, a half-opening angle θ is inferred for each source of the ES using Eq. 9. The values of θ are listed in Table 2. Fig. 7a shows the probability distribution of the half-opening angle θ within the ES. The blue solid line represents a logarithmic normal distribution, which best fits the data. This distribution has a mode of $Mo_\theta = 17.62^\circ$, a mean of $\mu_\theta = 30.05^\circ$, a median of $Me_\theta = 25.15^\circ$, and a standard deviation of $\sigma_\theta = 19.65^\circ$. Moreover, it is possible to verify that, by correcting the L_{rf}^{iso} light curve of each ES source for its corresponding θ , an overlap of the LXRE luminosity light curves as good as the one seen in the GS by Pisani et al. (2013) shown in Fig. 2 is obtained. Since the LXRE follows a power law behavior, we can quantify the tightness of the LXREs overlap looking at the correlation coefficient ρ between all the luminosity light-curve data points of the ES sources in log-log scale. Considering the data points of the LXRE power laws within the 10^4 – 10^6 s time interval (where we have defined E_{LT}), we obtain $\rho = -0.94$ for the GS, $\rho = -0.84$ for the ES before the collimation correction, and $\rho = -0.97$ after the correction. Therefore, the collimation correction not only reduces the spread of the LXREs within the ES, but makes the LXREs overlap even tighter than the one previously found in the GS.

Finally, in order to test the robustness of our results, we do the same analysis excluding, by the ES, the sources seen only by *Swift*/BAT or HETE and not by *Fermi*/GBM or Konus-WIND, under the hypothesis that their E_{iso} estimates are unreliable. The results obtained using this new sample called ES2, namely the typical value and the dispersion of α , E_{LT} , and θ are summarized in Table 1. There is no significant difference between the results obtained from the two samples. Therefore, we conclude that a possible wrong estimate of E_{iso} for the sources observed by only *Swift*/BAT or HETE and not by *Fermi*/GBM or Konus-WIND does not bias our results.

4. INFERENCES FOR THE UNDERSTANDING OF THE X-RAY AFTERGLOW STRUCTURE

In the last 25 years we have seen in the GRB community a dominance of the fireball model, which sees

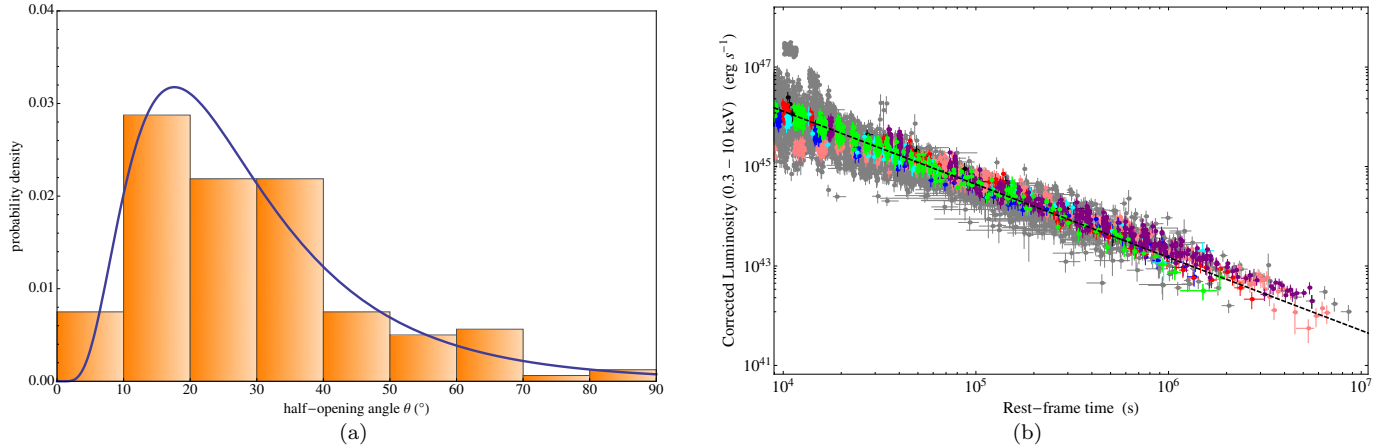


Figure 7. Left panel (a): probability distribution of the half-opening angle θ within the ES. The blue solid line represents a logarithmic normal distribution, which best fits the data. This distribution has a mode of $Mo_{\theta} = 17.62^{\circ}$, a mean of $\mu_{\theta} = 30.05^{\circ}$, a median of $Me_{\theta} = 25.15^{\circ}$, and a standard deviation of $\sigma_{\theta} = 19.65^{\circ}$. Right panel (b): corrected LXRE luminosity light curves of all 161 sources of the ES (gray) compared to the ones of the GS: GRB 060729 (pink), GRB 061007 (black), GRB 080913B (blue), GRB 090618 (green), GRB 091127 (red), and GRB 111228 (cyan), plus GRB 130427A (purple; Pisani et al. 2013; Ruffini et al. 2015). The black dotted line represents the universal LXRE power law, namely the linear fit of the late emission of GRB 050525A.

Table 1

Summary of the results of this work obtained by the complete ES sample in comparison with the ones arising using the sample ES2, namely the ES deprived by the sources seen by *Swift*/BAT or HETE only.

Sample	ES	ES2
Sources Number	161	102
α	1.48 ± 0.32	1.45 ± 0.24
$\text{Log}_{10}(E_{LT}/\text{erg})$	51.40 ± 0.47	51.47 ± 0.48
θ ($^{\circ}$)	30.05 ± 19.65	28.26 ± 17.85
θ mode ($^{\circ}$)	17.62	17.08
θ median ($^{\circ}$)	25.15	23.90

the GRB as a single astrophysical system, the ‘‘Collapsar’’, originating from an ultra-relativistic jetted emission described by the synchrotron/self-synchrotron Compton (SSC) and traditional afterglow models (see, e.g. Woosley 1993; Rees & Meszaros 1992; Piran 2005; Gehrels et al. 2009; Kumar & Zhang 2015, and references therein). Such methods have been systematically adopted to different types of GRBs like, for example, the short, hard GRB 090510 (Ackermann et al. 2010), the high energetic long GRB 130427A (Perley et al. 2014), the low energetic short GRB 051221A (Soderberg et al. 2006b), and the low energetic long GRB 060218 (Campana et al. 2006; Soderberg et al. 2006a), independently from the nature of their progenitors.

In the recent four years, substantial differences among seven distinct kinds of GRBs have been indicated, presenting different spectral and photometrical properties on different time scales (Ruffini et al. 2016c). The discovery of several long GRBs showing multiple components and evidencing the presence of a precise sequence of different astrophysical processes during the GRB phenomenon (e.g. Izzo et al. 2012b; Penacchioni et al. 2012), led to the introduction of a novel paradigm explicating the role of binary sources as progenitors of the long GRB-SN connection. This has led to the formulation of the IGC paradigm (Ruffini et al. 2001b, 2007; Izzo et al. 2012a; Rueda & Ruffini 2012; Fryer et al. 2014; Ruffini et al. 2015). Within the IGC paradigm, a tight binary system composed of a carbon-oxygen core (CO_{core}) un-

dergoing a supernova (SN) explosion in the presence of a binary NS companion has been suggested as the progenitor for long gamma-ray bursts. Different scenarios occur depending on the distance between the CO_{core} and the NS binary companion (Becerra et al. 2015). Correspondingly two different sub-classes of long bursts have been shown to exist (for details, see Ruffini et al. 2015, 2016c). A first long burst sub-class occurs when the CO_{core} -NS binary separation a is so large (typically $a > 10^{11}$ cm, see, e.g., Becerra et al. (2015) that the accretion of the SN ejecta onto the NS is not sufficient to have the NS reach its critical mass, M_{crit} , for gravitational collapse to a BH to occur. The hypercritical accretion of the SN ejecta onto the NS binary companion occurs in this case at rates below 10^{-2} solar masses per second and is characterized by a large associated neutrino emission (Zel’dovich et al. 1972; Ruffini & Wilson 1973; Rueda & Ruffini 2012; Fryer et al. 2014). We refer to such systems as X-ray flashes (XRFs). A second long burst subclass occurs when the CO_{core} -NS binary is more tightly bound ($a < 10^{11}$ cm, see, e.g., Becerra et al. (2015). The larger accretion rate of the SN ejecta, e.g., 10^{-2} - 10^{-1} solar masses per second, leads the companion NS to easily reach its critical mass M_{crit} (Rueda & Ruffini 2012; Fryer et al. 2014; Becerra et al. 2015), leading to the formation of a BH. We refer to such systems as binary-driven hypernovae (BdHNe, see, e.g., Ruffini et al. 2014c, 2015). A main observational feature, which allows us to differentiate BdHNe from XRFs is the isotropic γ -ray energy E_{iso} being larger than 10^{52} erg. Such a separation energy value is intimately linked to the binary separation a of the binary progenitor and the consequent birth or not of the BH (for details, see Ruffini et al. 2016c).

Thanks to the XRT instrument on board the *Swift* satellite (Gehrels et al. 2004; Evans et al. 2007, 2010), we can compare and contrast the X-ray afterglow emissions of BdHNe and XRFs (see Fig. 8). The typical X-ray afterglows of XRFs can be divided into two main parts: an initial bump with rapid decay, followed by an emerging slight decaying power law (see Fig. 8). The typical X-ray afterglow light curve of BdHNe can be divided into three different parts: (1) an initial spike followed by an early

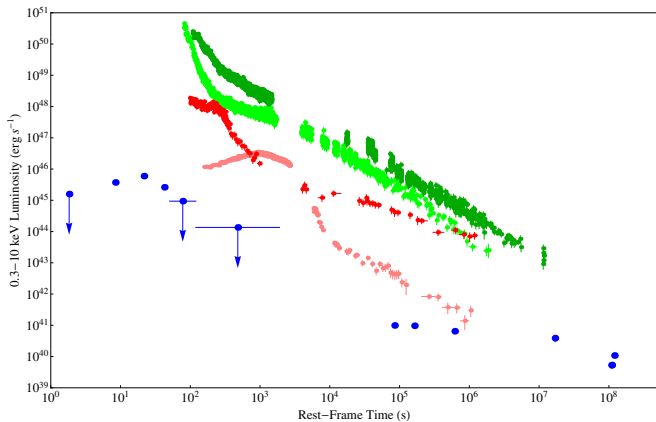


Figure 8. Comparison between rest-frame luminosity light curves of proto-typical BdHNe and XRFs sources. The BdHNe shown are GRB 130427A (dark green) and GRB 090618 (light green); while the XRF shown are GRB 101219B (red), GRB 060218 (pink), and GRB 980425 (blue).

steep power law decay; (2) a plateau phase; and (3) a late power law decay, the LXRE, which is the presented in this work (Ruffini et al. 2015; Nousek et al. 2006). The treatment of the first parts of the X-ray afterglow of BdHNe, namely the spike, the initial steep decay, and the plateau phase, indeed fundamental within the BdHN picture, is beyond the scope of this article and it will be extensively shown in forthcoming works (Ruffini et al. 2016a,b, both in preparation).

The universalities of the LXRE outlined in this article are then explained within the IGC paradigm, originating from the interaction of the GRB with the SN ejecta. The constancy of the late power law luminosity in the rest frame is now explained in terms of the constancy in mass of the SN ejecta, which is standard in a BdHN (Rueda & Ruffini 2012; Fryer et al. 2014; Becerra et al. 2015).

It is appropriate to point out that no achromatic “Jet-break” effect has been observed in any of the 161 sources of our ES. We recall that the achromatic “Jet-break” effect is a consequence of relativistic jet pictures (Lorentz factor $\Gamma \sim 100-200$), in which a change of slope is expected in the late X-ray light curve (see e.g. Woosley 1993; Rees & Meszaros 1992; Piran 2005; Gehrels et al. 2009; Kumar & Zhang 2015, and references therein), which clearly does not apply in the case of the BdHN following the IGC model. In this scenario, a velocity of expansion $v \sim 0.8c$ (Lorentz factor $\Gamma \sim 2$) is found, indicating that the collimation of the SN ejecta originates in a mildly relativistic regime (Ruffini et al. 2014c, 2015). This cannot be related to the ultra-relativistic jet emission recalled above, considered in the early work of Frail et al. (2001) and continued all the way to the more recent results presented by Ghirlanda et al. (2013). These authors attempted to explain all GRBs as originating from a single object with an intrinsic energy approximately of 10^{50} erg (Frail et al. 2001) or 10^{48} erg (Ghirlanda et al. 2013): the different energetics and structures of all the GRBs were intended to be explained by the beaming effect with different ultra-relativistic Lorentz factors $\Gamma \sim 100-200$. Indeed, it is by now clear (see Ruffini et al. 2015, 2016c) that at least seven different classes of GRBs exist, each with different progenitors, different energies, and different spectra. In no way these distinct classes can be explained by a single common progenitor,

using simply relativistic beaming effects.

5. CONCLUSIONS

In this work, we give new statistical evidence for the existence of a universal behavior for the LXREs of BdHNe, introducing the presence of a collimation effect in such emission, and presenting the common LXRE energy $E_{LT}^{intr} = E_{LT}^{050525A} = 2.43 \times 10^{50}$ as a standard candle. We build an “enlarged sample” (ES) of 161 BdHNe, and focus on their LXREs and then we introduce a collimation effect. These analyses lead us to the following results.

1) We find for the ES an increased variability in the decaying LXRE power law behavior in respect to the result previously deduced by Pisani et al. (2013). The typical slope of the power law characterizing the LXRE is $\alpha = 1.48 \pm 0.32$ (GS: $\alpha = 1.44 \pm 0.18$), while the late-time integrated luminosity between 10^4-10^6 seconds in the rest frame is $\text{Log}_{10}(E_{LT}/\text{erg}) = 51.40 \pm 0.47$ (GS: $\text{Log}_{10}(E_{LT}/\text{erg}) = 51.15 \pm 0.28$).

2) The introduction of a collimation in the LXRE recovers a universal behavior. Assuming a double-cone shape for the LXRE region, we obtain a distribution of half-opening angles peaking at $\theta = 17.62^\circ$, with a mean value of 30.05° , and a standard deviation of 19.65° , see Fig. 7a.

3) The application of the collimation effect to the LXREs of the ES indeed reduces the scattering of the power law behavior found under the common assumption of isotropy; see Fig. 5a-b. The power law scattering of the LXREs, after being corrected by the collimation factor, results in being even lower than the one found in the GS; see Fig. 7b.

The fact that these extreme conditions neither were conceived nor are explained within the traditional ultra-relativistic jetted SSC model (see, e.g. Woosley 1993; Rees & Meszaros 1992; Piran 2005; Gehrels et al. 2009; Kumar & Zhang 2015, and references therein), in view also of the clear success of the IGC paradigm in explaining the above features, comes as a clear support to a model for GRBs strongly influenced by the binary nature of their progenitors, involving a definite succession of selected astrophysical processes for a complete description of the BdHNe.

These intrinsic signatures in the LXREs of BdHNe, independent from the energetics of the GRB prompt emission, open the perspective for a standard candle up to $z \gtrsim 8$.

It is remarkable that the universal behavior occurs in the rest-frame time interval 10^4-10^6 s, which precisely corresponds to the temporal window of the early observations of Beppo-SAX at the time of the afterglow discovery (see Fig 1).

We thank both the editor and the referee for the fruitful correspondence that improved the presentation of our results. This work made use of data supplied by the UK Swift Science Data Center at the University of Leicester. J. A. R. acknowledges the support by the International Cooperation Program CAPES-ICRANet financed by CAPES-Brazilian Federal Agency for Support and Evaluation of Graduate Education within the Ministry of Education of Brazil. M. K. and Y. A. ac-

knowledge the support given by the International Relativistic Astrophysics Erasmus Mundus Joint Doctorate Program under the Grants 20131471 and 20140707, respectively, from EACEA of the European Commission. M. M. acknowledges the partial support of the project No. 3101/GF4 IPC-11/2015, and the target program of the Ministry of Education and Science of the Republic of Kazakhstan.

REFERENCES

- Ackermann, M., Asano, K., Atwood, W. B., et al. 2010, *ApJ*, 716, 1178
- Becerra, L., Cipolletta, F., Fryer, C. L., Rueda, J. A., & Ruffini, R. 2015, *ApJ*, 812, 100
- Bloom, J. S., Frail, D. A., & Sari, R. 2001, *AJ*, 121, 2879
- Boella, G., Butler, R. C., Perola, G. C., et al. 1997, *A&AS*, 122
- Campana, S., Mangano, V., Blustin, A. J., et al. 2006, *Nature*, 442, 1008
- Costa, E., Frontera, F., Heise, J., et al. 1997a, *Nature*, 387, 783
- Costa, E., Feroci, M., Piro, L., et al. 1997b, *IAU Circ.*, 6576
- de Pasquale, M., Piro, L., Gendre, B., et al. 2006, *A&A*, 455, 813
- de Ugarte Postigo, A., Xu, D., Leloudas, G., et al. 2013, *GCN Circ.*, 14646, 1
- Della Valle, M., Malesani, D., Benetti, S., et al. 2006a, *IAU Circ.*, 8696
- Della Valle, M., Malesani, D., Bloom, J. S., et al. 2006b, *ApJ*, 642, L103
- Dezalay, J.-P., Barat, C., Talon, R., et al. 1992, in *American Institute of Physics Conference Series*, Vol. 265, American Institute of Physics Conference Series, ed. W. S. Paciesas & G. J. Fishman, 304–309
- Evans, P. A., Beardmore, A. P., Page, K. L., et al. 2007, *A&A*, 469, 379
- Evans, P. A., Willingale, R., Osborne, J. P., et al. 2010, *A&A*, 519, A102
- Frail, D. A., Kulkarni, S. R., Sari, R., et al. 2001, *ApJ*, 562, L55
- Frontera, F., Costa, E., Piro, L., et al. 1998, *ApJ*, 493, L67
- Frontera, F., Amati, L., Costa, E., et al. 2000, *ApJSS*, 127, 59
- Fryer, C. L., Rueda, J. A., & Ruffini, R. 2014, *ApJ*, 793, L36
- Gehrels, N., Ramirez-Ruiz, E., & Fox, D. B. 2009, *ARAA*, 47, 567
- Gehrels, N., Chincarini, G., Giommi, P., et al. 2004, *ApJ*, 611, 1005
- Ghirlanda, G., Ghisellini, G., Salvaterra, R., et al. 2013, *MNRAS*, 428, 1410
- Golenetskii, S., Aptekar, R., Mazets, E., et al. 2005, *GRB Coordinates Network*, 3474
- Izzo, L., Rueda, J. A., & Ruffini, R. 2012a, *A&A*, 548, L5
- Izzo, L., Ruffini, R., Penacchioni, A. V., et al. 2012b, *A&A*, 543, A10
- Klebesadel, R. W. 1992, in *Gamma-Ray Bursts - Observations, Analyses and Theories*, ed. C. Ho, R. I. Epstein, & E. E. Fenimore (Cambridge University Press), 161–168
- Kouveliotou, C., Meegan, C. A., Fishman, G. J., et al. 1993, *ApJ*, 413, L101
- Kumar, P., & Zhang, B. 2015, *Phys. Rep.*, 561, 1
- Levan, A. J., Fruchter, A. S., Graham, J., et al. 2013, *GCN Circ.*, 14686, 1
- Margutti, R., Zaninoni, E., Bernardini, M. G., et al. 2013, *MNRAS*, 428, 729
- Mazets, E. P., Golenetskii, S. V., Ilinskii, V. N., et al. 1981, *Ap&SS*, 80, 3
- Meszáros, P., & Rees, M. J. 1997, *ApJ*, 476, 232
- Nousek, J. A., Kouveliotou, C., Grupe, D., et al. 2006, *ApJ*, 642, 389
- Penacchioni, A. V., Ruffini, R., Bianco, C. L., et al. 2013, *A&A*, 551, A133
- Penacchioni, A. V., Ruffini, R., Izzo, L., et al. 2012, *A&A*, 538, A58
- Perley, D. A., Cenko, S. B., Corsi, A., et al. 2014, *ApJ*, 781, 37
- Piran, T. 2005, *Rev. Mod. Phys.*, 76, 1143
- Pisani, G. B., Izzo, L., Ruffini, R., et al. 2013, *A&A*, 552, L5
- Rees, M. J., & Meszáros, P. 1992, *MNRAS*, 258, 41P
- Rueda, J. A., & Ruffini, R. 2012, *ApJ*, 758, L7
- Ruffini, R., Bianco, C. L., Chardonnet, P., Fraschetti, F., & Xue, S.-S. 2001a, *ApJ*, 555, L107
- 2001b, *ApJ*, 555, L113
- 2001c, *ApJ*, 555, L117
- Ruffini, R., & Wilson, J. 1973, *Physical Review Letters*, 31, 1362
- Ruffini, R., Bernardini, M. G., Bianco, C. L., et al. 2007, *ESA SP*, 622, 561
- Ruffini, R., Bianco, C. L., Enderli, M., et al. 2013a, *GCN Circ.*, 14526, 1
- 2013b, *GRB Coordinates Network*, 14888
- 2013c, *GRB Coordinates Network*, 15576
- 2014a, *GRB Coordinates Network*, 15707
- Ruffini, R., Izzo, L., Muccino, M., et al. 2014b, *A&A*, 569, A39
- Ruffini, R., Muccino, M., Bianco, C. L., et al. 2014c, *A&A*, 565, L10
- Ruffini, R., Wang, Y., Enderli, M., et al. 2015, *ApJ*, 798, 10
- Ruffini, R., Wang, Y., Moradi, R., et al. 2016a, in preparation
- Ruffini, R., Rueda, J. A., Becerra, L. M., et al. 2016b, in preparation
- Ruffini, R., Rueda, J. A., Muccino, M., et al. 2016c, *ArXiv e-prints*: 1602.02732, *ApJ* in press
- Salvaterra, R., Della Valle, M., Campana, S., et al. 2009, *Nature*, 461, 1258
- Sari, R., Piran, T., & Narayan, R. 1998, *ApJ*, 497, L17
- Soderberg, A. M., Kulkarni, S. R., Nakar, E., et al. 2006a, *Nature*, 442, 1014
- Soderberg, A. M., Berger, E., Kasliwal, M., et al. 2006b, *ApJ*, 650, 261
- Tanvir, N. R., Fox, D. B., Levan, A. J., et al. 2009, *Nature*, 461, 1254
- Tavani, M. 1998, *ApJ*, 497, L21
- Woodsley, S. E. 1993, *ApJ*, 405, 273
- Zel’dovich, Y. B., Ivanova, L. N., & Nadezhin, D. K. 1972, *Soviet Ast.*, 16, 209

Table 2 List of the the ES of BdHNe considered in this work. It is composed by 161 sources spanning 11 years of Swift/XRT observation activity. In the table we report important observational features: the redshift z , our estimates of the LXRE power-law slope α , the late times energy E_{LT} , the collimation half-opening angle θ , the isotropic energy E_{iso} of the GRB, the observing instrument in the γ -ray band, and the correspondent circular (GCN) from which we take the γ -ray spectral parameters in order to estimate the E_{iso} of the GRB source.

(a): in units of 10^{51} erg.

(b): in units of 10^{52} erg.

(c): “Swift” stays for *Swift*/BAT; “Fermi” stays for *Fermi*/GBM; “KW” stays for Konus-WIND.

GRB	z	α	$E_{LT}^{(a)}$	θ ($^\circ$)	$E_{iso}^{(b)}$	Instrument ^(c)	GCN
050315A	1.95	0.838	15.6	10.1	8.32	Swift	3099
050318A	1.44	1.74	0.442	63.3	3.70	Swift	3134
050319A	3.24	1.27	12.3	11.4	20.2	Swift	3119
050401A	2.9	1.59	3.82	20.6	92.0	KW	3179

Table 2 continued.

GRB	z	α	$E_{LT}^{(a)}$	θ ($^\circ$)	$E_{iso}^{(b)}$	Instrument ^(c)	GCN
050408A	1.24	1.14	2.19	27.2	10.8	HETE	3188
050505A	4.27	1.41	8.66	13.6	44.6	Swift	3364
050525A	0.606	1.47	0.243	90.0	2.31	KW	3474
050730A	3.97	2.42	1.74	30.7	42.8	Swift	3715
050802A	1.71	1.55	1.24	36.5	7.46	Swift	3737
050814A	5.3	2.23	2.90	23.6	26.8	Swift	3803
050820A	2.61	1.23	22.1	8.51	39.0	KW	3852
050922C	2.2	1.57	0.974	41.4	19.8	KW	4030
051109A	2.35	1.20	9.09	13.3	18.3	KW	4238
060108A	2.03	0.830	3.40	21.8	1.50	Swift	4445
060115A	3.53	1.58	2.23	27.0	19.0	Swift	4518
060124A	2.296	1.30	20.7	8.79	26.0	KW	4599
060202A	0.783	1.03	4.57	18.8	1.90	Swift	4635
060206A	4.05	1.44	28.8	7.45	3.90	Swift	4697
060210A	3.91	1.75	25.9	7.86	120.	Swift	4734
060418A	1.49	1.54	0.614	52.9	12.0	KW	4989
060502A	1.51	1.26	2.96	23.4	11.0	Swift	5053
060510B	4.9	1.54	3.39	21.8	66.0	Swift	5107
060512A	2.1	1.24	0.356	71.5	2.38	Swift	5124
060526A	3.21	2.27	1.36	34.7	5.40	Swift	5174
060605A	3.8	2.00	0.524	57.6	10.1	Swift	5231
060607A	3.082	3.04	0.481	60.4	34.0	Swift	5242
060707A	3.43	1.18	11.4	11.8	5.30	Swift	5289
060708A	1.92	1.21	1.22	36.8	2.20	Swift	5295
060714A	2.71	1.47	1.93	29.0	19.0	Swift	5334
060729A	0.54	1.31	3.36	21.9	1.60	Swift	5370
060814A	0.84	1.16	1.69	31.1	6.30	KW	5460
060906A	3.685	1.47	0.482	60.3	25.9	Swift	5534
061007A	1.261	1.68	0.477	60.6	88.0	KW	5722
061121A	1.314	1.50	3.75	20.7	27.0	KW	5837
061126A	1.159	1.30	3.06	23.0	8.10	Swift	5860
061222A	2.088	1.52	18.7	9.25	33.0	KW	5984
070110A	2.35	1.10	3.20	22.5	11.9	Swift	6007
070306A	1.5	1.58	8.22	14.0	15.5	Swift	6173
070318A	0.84	1.42	1.97	28.8	4.37	Swift	6212
070508A	0.82	1.60	1.08	39.1	7.57	KW	6403
070529A	2.5	1.22	1.79	30.2	31.9	Swift	6468
070802A	2.45	1.41	0.633	52.0	1.64	Swift	6699
071003A	1.6	1.75	1.61	31.9	35.8	KW	6849
080210A	2.64	1.38	1.26	36.2	11.8	Swift	7289
080310A	2.43	1.53	1.34	35.1	20.0	Swift	7402
080319B	0.94	1.59	1.99	28.6	122.	KW	7482
080319C	1.95	1.72	6.40	15.8	14.6	KW	7487
080605A	1.64	1.59	1.39	34.5	22.1	KW	7854
080607A	3.04	1.57	1.77	30.4	187.	KW	7862
080721A	2.6	1.62	8.93	13.4	132.	KW	7995
080804A	2.2	1.68	1.08	39.3	56.9	Swift	8067
080805A	1.51	1.07	1.21	36.9	9.96	Swift	8068
080810A	3.35	1.57	1.77	30.4	76.1	KW+Swift	8101
080905B	2.37	1.51	4.67	18.6	9.85	Fermi	8205
080916C	4.35	1.29	12.1	11.5	242.	Fermi	8278
080928A	1.69	1.69	0.564	55.3	4.93	Fermi	8316
081008A	1.97	1.80	0.596	53.7	9.34	Swift	8351
081028A	3.04	1.66	2.62	24.9	12.0	Swift	8428
081109A	0.98	1.32	1.07	39.4	1.87	Fermi	8505
081121A	2.51	1.51	5.77	16.7	24.9	Fermi	8546
081203A	2.1	2.00	0.446	63.0	35.1	Swift	8595
081221A	2.26	0.849	24.5	8.09	33.8	Fermi	8704
081222A	2.77	1.40	4.28	19.4	25.9	Fermi	8715
090102A	1.55	1.35	1.58	32.2	19.8	KW	8776
090313A	3.38	2.72	10.4	12.4	13.1	Swift	8986
090328A	0.736	1.84	1.42	34.0	19.5	Fermi	9056
090418A	1.61	1.68	0.967	41.5	15.0	KW	9171
090423A	8.2	1.57	1.29	35.7	10.9	Fermi	9229
090424A	0.544	1.18	1.76	30.5	4.51	Fermi	9230
090516A	3.9	1.40	4.52	18.9	65.0	Fermi	9413
090618A	0.54	1.49	1.44	33.8	25.4	Fermi	9535
090715B	3.	1.18	4.08	19.9	22.1	KW	9679

Table 2 continued.

GRB	z	α	$E_{LT}^{(a)}$	θ ($^\circ$)	$E_{iso}^{(b)}$	Instrument ^(c)	GCN
090809A	2.74	1.57	0.727	48.3	4.98	Swift	9756
090812A	2.45	1.23	5.39	17.3	41.7	KW+Swift	9821
090902B	1.82	1.22	6.15	16.2	403.	Fermi	9866
090926A	2.11	1.50	5.29	17.4	217.	Fermi	9933
091003A	0.9	1.36	1.32	35.3	10.9	Fermi	9983
091020A	1.71	1.30	2.19	27.3	7.63	Fermi	10095
091029A	2.75	1.60	5.81	16.6	7.52	Swift	10103
091127A	0.49	1.32	1.36	34.9	1.79	Fermi	10204
091208B	1.06	1.09	1.15	38.0	2.03	Fermi	10266
100302A	4.81	0.812	5.67	16.8	5.24	Swift	10462
100425A	1.75	1.20	0.767	46.9	2.84	Swift	10685
100513A	4.77	1.44	3.74	20.8	25.7	Swift	10753
100621A	0.542	1.12	8.52	13.7	6.93	KW	10882
100814A	1.44	1.64	14.3	10.6	15.8	Fermi	11099
100901A	1.41	1.36	7.89	14.3	8.09	Swift	11169
100906A	1.73	1.87	1.32	35.3	22.5	Fermi	11248
110128A	2.339	1.16	0.620	52.6	3.60	Fermi	11628
110205A	2.22	1.59	0.913	42.8	41.0	KW	11659
110213A	1.46	1.81	2.33	26.4	7.00	Fermi	11727
110422A	1.77	1.24	6.03	16.3	62.0	KW	11971
110503A	1.613	1.36	2.45	25.7	19.0	KW	12008
110715A	0.82	1.69	7.33	14.8	5.60	KW	12166
110731A	2.83	1.22	6.31	16.0	42.0	Fermi	12221
110808A	1.348	1.33	0.588	54.1	6.10	Swift	12262
110918A	0.982	1.64	19.5	9.07	190.	KW	12362
111008A	4.9898	1.66	8.76	13.5	82.0	KW	12433
111123A	3.1516	1.55	2.82	24.0	70.0	Swift	12598
111209A	0.67	1.54	1.45	33.6	67.0	KW	12663
111228A	0.716	1.23	1.24	36.4	4.10	Fermi	12744
120119A	1.73	1.28	1.68	31.2	37.5	Fermi	12874
120326A	1.8	1.87	9.97	12.7	3.70	Fermi	13145
120327A	2.81	1.58	1.33	35.1	36.5	Swift	13137
120711A	1.41	1.58	18.1	9.40	166.	Fermi	13437
120712A	4.17	1.37	2.90	23.7	18.3	Fermi	13469
120909A	3.93	1.30	11.8	11.7	73.2	Fermi	13737
120922A	3.1	1.19	5.41	17.3	32.0	Fermi	13809
121024A	2.3	1.44	1.18	37.4	10.7	Swift	13899
121027A	1.77	1.28	15.8	10.1	6.55	Swift	13910
121128A	2.2	1.48	1.85	29.7	13.2	Fermi	14012
121217A	3	1.26	30.6	7.23	24.2	Fermi	14094
130418A	1.218	1.52	0.265	85.4	9.90	KW	14417
130420A	1.297	1.25	1.32	35.4	7.74	Fermi	14429
130427A	0.338	1.26	4.17	19.7	105.	Fermi	14473
130427B	2.78	1.85	0.275	83.4	5.04	Swift	14469
130505A	2.27	1.50	16.0	10.0	347.	KW	14575
130514A	3.6	1.56	5.16	17.7	52.4	KW+Swift	14702
130528A	1.25	1.02	2.03	28.3	4.40	Fermi	14729
130606A	5.91	1.91	1.24	36.4	28.3	KW	14808
130610A	2.092	1.47	0.472	61.0	6.99	Fermi	14858
130701A	1.155	1.20	0.639	51.7	2.60	KW	14958
130907A	1.238	1.68	7.02	15.1	304.	KW	15203
130925A	0.347	1.32	2.85	23.8	18.4	Fermi	15255
131030A	1.293	1.27	2.97	23.4	173.	KW	15413
131105A	1.686	1.24	1.75	30.6	34.7	Fermi	15455
131108A	2.4	1.72	0.932	42.3	73.0	Fermi	15477
131117A	4.042	1.31	0.816	45.4	1.02	Swift	15499
131231A	0.642	1.44	3.39	21.8	22.2	Fermi	15644
140206A	2.74	1.43	13.5	10.9	35.9	Fermi	15796
140213A	1.2076	2.21	16.2	9.94	9.93	Fermi	15833
140226A	1.98	1.58	0.762	47.1	5.80	KW	15889
140304A	5.283	1.44	7.14	15.0	13.7	Fermi	15923
140311A	4.954	1.49	1.18	37.5	11.6	Swift	15962
140419A	3.956	1.84	9.32	13.1	186.	KW	16134
140423A	3.26	1.31	4.11	19.8	65.3	Fermi	16152
140506A	0.889	0.924	2.78	24.2	1.12	Fermi	16220
140508A	1.027	1.40	5.46	17.2	23.9	Fermi	16224
140509A	2.4	1.46	0.402	66.7	9.14	Swift	16240
140512A	0.725	1.62	2.22	27.1	7.76	Fermi	16262

Table 2 continued.

GRB	z	α	$E_{LT}^{(a)}$	θ ($^\circ$)	$E_{iso}^{(b)}$	Instrument ^(c)	GCN
140614A	4.233	1.24	2.00	28.5	7.30	Swift	16402
140620A	2.04	1.43	5.16	17.7	6.22	Fermi	16426
140629A	2.275	1.48	0.868	44.0	6.15	KW	16495
140703A	3.14	2.21	1.82	30.0	1.72	Fermi	16512
140907A	1.21	0.888	2.68	24.6	2.29	Fermi	16798
141026A	3.35	2.24	34.8	6.78	7.17	Swift	16960
141109A	2.993	1.31	7.85	14.3	5.05	KW	17055
141121A	1.47	1.67	6.56	15.6	14.6	KW	17108
141221A	1.452	1.18	0.970	41.5	1.94	Fermi	17216
150206A	2.087	1.28	10.1	12.6	151.	KW	17427
150314A	1.758	1.57	3.08	22.9	98.1	Fermi	17579
150403A	2.06	1.61	26.7	7.74	91.0	Fermi	17674
150514A	0.807	1.35	0.378	69.1	1.14	Fermi	17819
150821A	0.755	1.20	0.884	43.5	15.1	Fermi	18190
150910A	1.36	1.50	0.415	65.6	22.3	Swift	18268
151021A	2.33	1.47	2.69	24.6	211.	KW	18433
151027A	0.81	1.69	2.04	28.3	3.86	Fermi	18492
151027B	4.063	1.75	4.19	19.6	19.1	Swift	18514
151111A	3.5	1.29	0.871	43.9	5.13	Fermi	18582
151112A	4.1	1.54	3.31	22.1	12.4	Swift	18593
151215A	2.59	1.07	1.34	35.1	1.97	Swift	18699